

Cellular Automaton experiments on local galactic structure.

II. Numerical simulations

A. Lejeune¹ and J. Perdang²

¹ Institut de Physique, Sart-Tilman, B-4000, Liège, Belgium

² Institute of Astronomy, Madingley Road, Cambridge CB3 0HA, UK, and Institut d'Astrophysique, 5, Avenue de Coïnte, B-4000 Liège, Belgium*

Received October 27, 1994; accepted March 6, 1996

Abstract. — This paper is a step towards demonstrating that the multi-parameter Cellular Automaton framework designed for the simulation of local galactic structure, developed in a companion paper (Perdang & Lejeune 1996, Paper I), is capable of duplicating the local irregularities observed in the structure of flocculent spiral galaxies. The numerical simulations exhibit the development of fractured galactic arms and the formation of fractal geometries associated with the matter distribution (fractal structure of the arms, of bulk dimension ≈ 1.7 and border dimension ≈ 1.3 ; distribution of different stellar components on fractal supports, of dimension ≈ 1.6 , for reasonable estimates of the free model parameters). The prediction of *fractional* values for the different *dimensions* specifying the simulated structures can be exploited as a qualitative test of adequacy of the proposed model. The precise quantitative values of the observed dimensions, in conjunction with the observable *global mass fractions* of the different galactic components, play the parts of constraints for the free model parameters. We show that the currently theoretically inaccessible values of the free parameters of the formulation can be recovered from observation.

Key words: galaxies: structure — star formation — methods: numerical — galaxies: evolution

1. Introduction

In this Paper we report on an extended series of numerical experiments carried out in the framework of a 2-dimensional *Cellular Automaton* (CA) model for local galactic structure described in the companion paper (Paper I). The model takes account of stellar evolutionary effects not dealt with in current CA models, as well as of quasi-stationary motions more complex than usual differential rotation. Our results are indicative that the floccular character of galaxies can be simulated in the CA framework.

For technical details of the implementation of the galactic physics we refer to Paper I. Our results are given in a relative reference frame F in uniform rotation with respect to the galaxy to be simulated.

2. Initial conditions. Remarks on infall and diffusion

In all of our experiments we start out with an initial diffuse non-uniform gas covering the part of the galaxy we are interested in (region Z over which the CA computations

are carried out). Any cell is either in the empty state E , or in the gas state D ; with the notations of Paper I

$$F(0; i, j) = 0 \text{ or } 1, \text{ for any cell } (i, j). \quad (2.1)$$

The choice between an E or a D state is made on the basis of a method reminiscent of a ‘mole’s labyrinth’ (Herrmann 1983), already adopted in previous CA simulations (Lejeune & Perdang 1991): The cells (in the auxiliary lattice L , cf. Paper I) are all provisionally populated with gas; a number of $b = 1, 2, \dots$ empty ‘bubbles’ are then generated by T -step random walks starting at b randomly chosen initial cells; for a selected number of different walks b , the number of steps T per walk is chosen such as to generate a preassigned fraction $f(E)$ of empty space in the lattice area; the remaining fraction of the area which is filled with gas is denoted $f(D) = 1 - f(E)$. Through the coordinate transformation Eq. (5.1a) of Paper I we obtain the initial state in the ‘physical’ zone Z (the lattice L'). Figure 1 provides a realisation of an initial configuration (corresponding to the velocity field of Fig. 3 of Paper I).¹

Send offprint requests to: A. Lejeune

*Permanent address

¹The purpose of this operation is to create an irregular cloudy shape, a locally non-uniform initial matter distribution de-

A special simulation should be included in our program to handle the internal dynamics of molecular clouds responsible for the formation of the complexity of the actual cloud shapes. The random walk procedure as adopted here should be viewed as a cheap substitute for simulating the observed fragmented gas cloud border. Incidentally, the numerical estimate of the fractal dimension (≈ 1.3) of the border of our simulated cloud in Fig. 1 compares favourably with the reported estimates of the fractal dimensions of cloud contours.

We note also that with our algorithm the gas area is either *connected* or it is *disconnected*, depending on whether or not the ‘empty bubble’ extends from the left to the right border of our zone Z ; provided that infall and diffusion are weak enough, connectivity is preserved at any later time. Under the first alternative a signal in one cell of the gas zone can propagate over the whole zone, i.e. the state of any cell (i, j) at a given timestep τ can influence the state of any other cell (i', j') at some later time τ' ; under the second alternative disconnected areas evolve independently.

Infall, as handled in the present simulation (Reaction (6.12) of Paper I) may generate a large number of D cells within the empty bubbles during the initial stages ($T_{\text{inf}} \approx 100$ timesteps) over which we let it operate. If N_c ($\approx n_x^2, n_y$ number of cells in the y direction) denotes the total number of cells of our lattice ($\approx 10^6$), a rough estimate of the number of these new gas cells $N(D)$ created by the implementation of infall is

$$N(D) \approx N_c f(E) P(E; D) T_{\text{inf}}. \quad (2.2)$$

With the numerical values $f(E) \approx 0.25$, $P(E; D) = 1 \times 10^{-5}$, we have $N(D)/N_c \approx 2.5 \times 10^{-4} \ll 1$, indicating that this mechanism should not play a significant evolutionary role.²

The action of *diffusion* in the framework of our simulation is more complex. On the computational level of the individual cellstates $F(\tau; i, j)$ (exhibited in Fig. 1a for an initial state, and in Fig. 3 for a later evolutionary phase), the diffusive mechanism detaches border gas cells, thereby creating new disconnected patches of matter. However, on a macroscopic, observationally meaningful ‘hydrodynamic scale’, simulated in our experiments by spatial smoothing (Fig. 1b; compare also Fig. 4), the averaged patches remain connected to the main clouds.

void of any particular symmetry (cf. also the procedure of Heisenberg & von Weizsäcker 1948). The random walk method was chosen in our experiments since it is particularly easy to implement. A more evolved CA approach capable of generating a variety of growth patterns, including realistic cloud shapes, has been developed recently by one of us (Perchang 1996).

²In order to lead to the formation of a single connected gas zone, and hence, in order to play a dominant part in the overall evolution, the characteristic time over which the infall should be operative, T_{inf}^* , should obey $T_{\text{inf}}^* \approx \frac{1}{f(E)P(E;D)}$.

In a T -step random walk the distance $r(T)$ a particle traverses on average, as estimated by the expectation E of $r(T)^2$ is

$$E(r(T)^2) \approx p_{\text{diff}} T \quad (2.3)$$

in units of the cellsize (p_{diff} , diffusion probability factor as implemented in our program). Hence, even for the strongest possible diffusion, ($p_{\text{diff}} = 1$), over a timescale T ($\approx 10^3$, for a typical evolutionary run), the average distance (2.3), in units of the total size of the CA network is

$$[E(r(T)^2)]^{1/2}/n_y \approx (T/N_c)^{1/2}, \quad (2.3a)$$

$\approx 3 \cdot 10^{-2} \ll 1$ for our experiments. Diffusion, therefore, although not completely negligible, cannot play a dominating part in our model. In the hydrodynamic representations (Fig. 4a) the effect of diffusion is obliterated for an averaging radius ρ obeying $\rho \geq \sqrt{\tau}$. This is indeed consistent with our experiments.³

Table 1 summarises the evolutionary reactions simulating the stellar evolutionary processes analysed in Paper I. The table also lists the corresponding independent transition probabilities per CA timestep (denoted here P_1, P_2, \dots, P_{15}) as adopted in our numerical experiments. Column (a) gives these parameter values for the galactic evolution from which we have constructed synthetic photographs. Column (b) corresponds to the reference ‘average’ model around which our calibration models for the coefficients in representations (3.3) and (4.4) are generated. Column (c) refers to one representative of the latter collection of models; it provides an indication of the range of model parameters explored in our experiments.

³The diffusion algorithm adopted in our program models *normal* diffusion, conforming to relation (2.3). For the purposes of simulating motions of real individual galactic components (proper motions of stars, for instance) normal diffusion appears to constrain too strongly the allowed velocities to constitute an acceptable model for the actual individual motions. We believe that a model of *anomalous diffusion* (or overdiffusion) could capture more adequately the physical situation. Anomalous diffusion could be implemented in principle (probabilistic displacement of a cell by a distance r obeying a Levy distribution; for the latter the asymptotic probability density for large displacements is of the form $1/r^{\mu+1}$, $0 < \mu < 2$; cf. Feller 1971). We have not attempted to incorporate this mechanism in our galactic model. We point out that for anomalous diffusion the variance of the displacement does not exist, as a consequence of the contribution of the large displacements per timestep. For this very reason anomalous diffusion secures a more efficient transport: the exponent 1/2 in the RHS of (2.3a) is to be replaced by $1/\mu$. It follows that provided that μ is taken small enough, anomalous diffusion can play a non-negligible part over timescales as dealt with in our experiments.

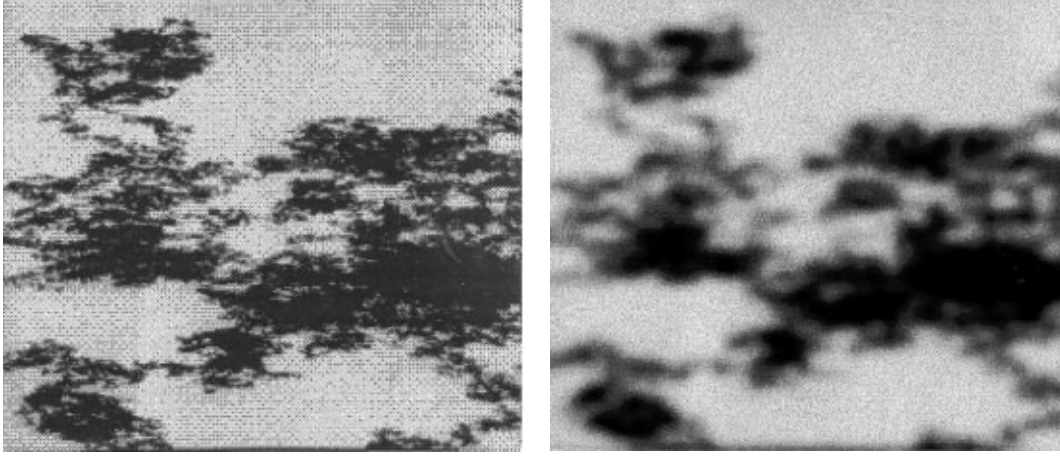


Fig. 1. a) An instance of an initial condition in lattice L' generated by a T -step random walk procedure ($10^3 \times 10^3$ embedding lattice, $T = 5 \cdot 10^6$) for the dynamics of Fig. 4; fractal dimension of border: 1.3. **b)** corresponding initial hydrodynamic state (averaging of **a**) over 31×31 cells). (black: empty cells; cyan: dust)

Table 1. Evolution rules and transition probabilities (Col. (a): synthetic photographs; Col. (c): reference model for calibration of Eqs. (3.3) and (4.4); Col. (c): another instance of the calibration models)

Reaction	Probability	(a)	(b)	(c)
Initial state: gas fraction		0.65	0.72	0.72
(1) Empty cells				
$E \rightarrow E$		1.	1.	1.
(2) Gas				
$D \rightarrow D$				
$D + dD \rightarrow P + dD$	P_1	0.00005	0.0005	0.0005
$D + dD \rightarrow L + dD$	P_2	0.00017	0.00017	0.00017
$D + pP + mM + rR \rightarrow P + pP + mM + rR$	P_3	0.020	0.100	0.300
(3) Protostars				
$P \rightarrow P$				
$P \rightarrow M$	P_4	0.0025	0.050	0.050
$P + mM + rR \rightarrow M + mM + rR$	P_5	0.0050	0.010	0.010
$P \rightarrow D$	P_6	0.090	0.180	0.180
$P + mM + rR \rightarrow D + mM + rR$	P_7	0.050	0.050	0.050
(4) Main sequence stars				
$M \rightarrow M$				
$M \rightarrow R$	P_8	0.0250	0.0250	0.0250
$M + rR \rightarrow R + rR$	P_9	0.0750	0.0750	0.2250
$M \rightarrow D$	P_{10}	0.0250	0.0250	0.0250
$M + mM + rR \rightarrow D + mM + rR$	P_{11}	0.0100	0.0100	0.0035
(5) Red giants				
$R \rightarrow R$				
$R \rightarrow D$	P_{12}	0.0980	0.0980	0.0980
$R \rightarrow I$	P_{13}	0.0005	0.0005	0.0005
(6) Low mass stars				
$L \rightarrow L$				
$L \rightarrow D$	P_{14}	0.	0.	0.
$L \rightarrow I$	P_{15}	0.000004	0.000004	0.000004

3. The global evolution of the galactic species

In Figs. 2 we exhibit several evolutionary sequences of the global mass fraction of our 6 galactic species. For the parameter ranges adopted, 3 phases can be distinguished:

(i) An initial short *transient phase*, characterised by a rapid building up of the protostar population and a corresponding decline of the amount of gas. This phase subdivides into a trigger-phase of star formation, of duration determined by the probability of the cloud collapse (P_1), followed in turn by a more violent star formation process of timescale fixed by the catalytic reaction probability (P_3). In Frame (a), corresponding to a large probability P_3 , we observe a prominent pulse of star formation of maximum at step 20; in Frame (b) the probability P_3 is reduced by a factor 2 and the pulse of star formation is virtually suppressed; in Frame (c), where P_3 is further reduced by a factor 2, the transient phase consists in a gentle rise of the protostar population over about 150 steps.

(ii) A subsequent *quasi-stationary phase* in the protostar, main sequence, and red giant population, during which the formation rates of these species are essentially balanced by their decay rates. The leakage of active galactic matter towards inert matter (and low mass stars, which play the part of inert matter as well within our numerical approximations) ultimately implies that the ‘source’ of protostars is progressively depleted; on average the protostar population is therefore bound to decrease. Frames (a) and (b) indicate that quasi-stationarity is practically realised beyond timestep ≈ 100 . In all cases the slow decrease due to loss of active matter can be approximated by a linear time behaviour.

(iii) Finally, our model conceals an *asymptotic equilibrium state*, for $\tau \rightarrow \infty$, in which all galactic matter is in the form of inert or low mass stars (if the transition probability $P(L; I)$ is set equal to zero). Practically this asymptotic state would be reached for evolutionary times τ_{as} such that $\tau_{\text{as}} P(D; L) > 1$, or $\tau_{\text{as}} P(A; B) > 1$, where $P(A; B)$ is the smallest transition probability in the global transformation sequence $D \rightarrow I$ via massive stars; in our numerical experiments this stage is never attained.⁴

We mention at this stage that depending on the precise parameter values, the quasi-stationary phase (ii) may exhibit different time patterns. Besides the *uniform decrease*, an *oscillatory* time-behaviour has been observed if the intermediate steps of the global reaction $D \rightarrow I$ are artificially set approximately equal. The low amplitude fluctuations observable in the D and P components of Fig. 2a may be a scar of such a periodic behaviour. Moreover, when instead of examining the space averaged global behaviour of the different species we examine the detailed spatial behaviour of the species, *spatial oscillations*

and *intermittency phenomena* are observed during the globally oscillatory phase. We have not followed up these types of complex behaviour in this paper.

In a mean field approximation, in which the space dependence is discarded, the global evolution equations reduce to simple iterative schemes (difference equations in time). Approximating the differences by differentials, we obtain ODEs for the evolution of the global population of the species, thereby reducing our original CA formulation to an elementary model of class (1) (Paper I). The resulting ODEs can be interpreted as evolution equations of chemical kinetics in a homogeneous medium; the kinetic equations are read off from the stoichiometric equations of Table 1. As already pointed out, the existence of oscillating solutions in these kinetic equations, for some range of the rate parameters, is well known: Standard chemical kinetics can give rise to stable oscillatory behaviour, provided that the reaction schemes involve a nonlinear feedback, in the form of catalytic processes.⁵

In the context of the CA model of GSS oscillatory behaviour is also encountered (cf. in particular Seiden & Schulman 1990 Fig. 16); the GSS oscillations appear in some range of a *refractory time*, or period of immunity of the gas against star formation; the latter plays the part of a formal substitute for the details of the ‘chemical kinetics’ we are adopting in our model.

In principle, the *relative populations* of the species (mass fractions), $N(Y; \tau; G) / \sum_Y N(Y; \tau; G) = a(Y; \tau; G)$, $Y = D, P, M, R, I, L$, over some large enough fixed area G of a galaxy, can be determined observationally at the present age of a galaxy τ_{gal} . Assuming that the galaxy is in a stable quasi-stationary phase (ii), we find from our numerical experiments that the relative populations are accurately represented in the form

⁵A triangular linear reaction scheme $A \rightarrow B; B \rightarrow C; C \rightarrow A$ shows an oscillatory behaviour if the 3 rates are identical (or sufficiently close); however, such an oscillation rapidly dies out and the system settles in a stable stationary state. The occurrence of a sustained oscillation around a stationary state requires this state to be unstable. Instability demands that the stationary state be on a ‘non-thermodynamic branch’, which is realised, in the chemical context, by catalytic and auto-catalytic steps (cf. Glansdorff & Prigogine 1971). The various catalytic steps in Table 1 were incorporated in our simulation precisely to investigate the possibility of ‘chemical instabilities’ within the reaction network of the galactic species. In our scheme, the quasi-stationary phase (ii) plays the part of a non-thermodynamic branch parametrised by the ‘secular time’. Asymptotically this branch merges with the thermodynamic equilibrium state, namely state (iii). Small deviations from the thermodynamic state inherit the stability of the latter, so that the oscillations can occur sufficiently far away from the asymptotic state (iii) only; this thermodynamic property implies that the oscillatory behaviour can survive over a finite ‘secular’ time only.

⁴A semi-analytic discussion of the general time behaviour based on an examination of the structure of the transition matrix is given in Perdang (1993 Sect. 5) for a more schematic version of the present model.

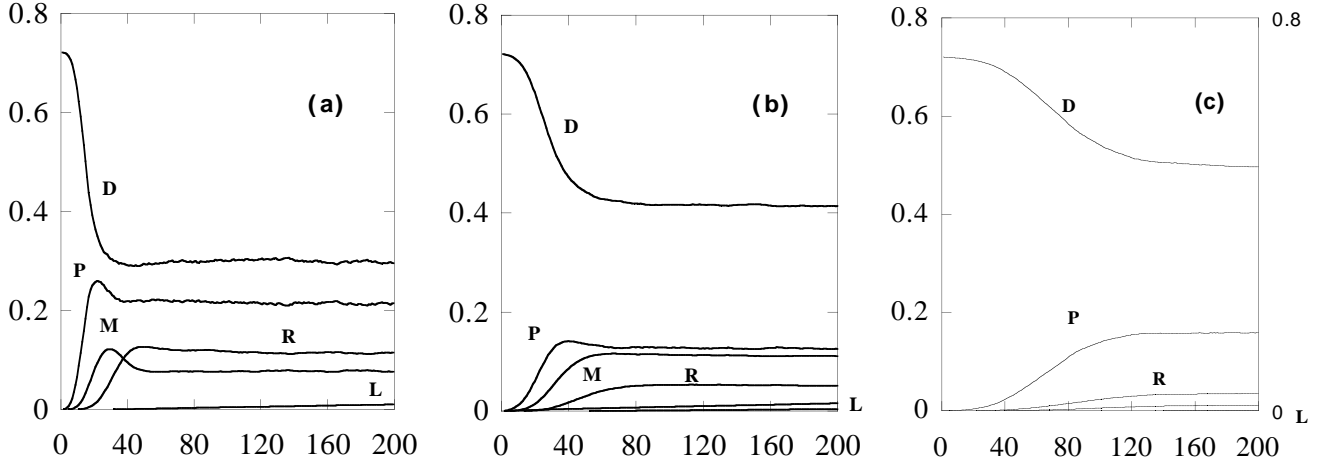


Fig. 2. Global evolution of the different galactic populations X for reference parameters of Table 1; $N(X; \tau; G)/N(G)$ represents fraction of galactic mass in form of species X at timestep τ averaged over whole lattice area G ($N(G)$, total number of initial gas cells)

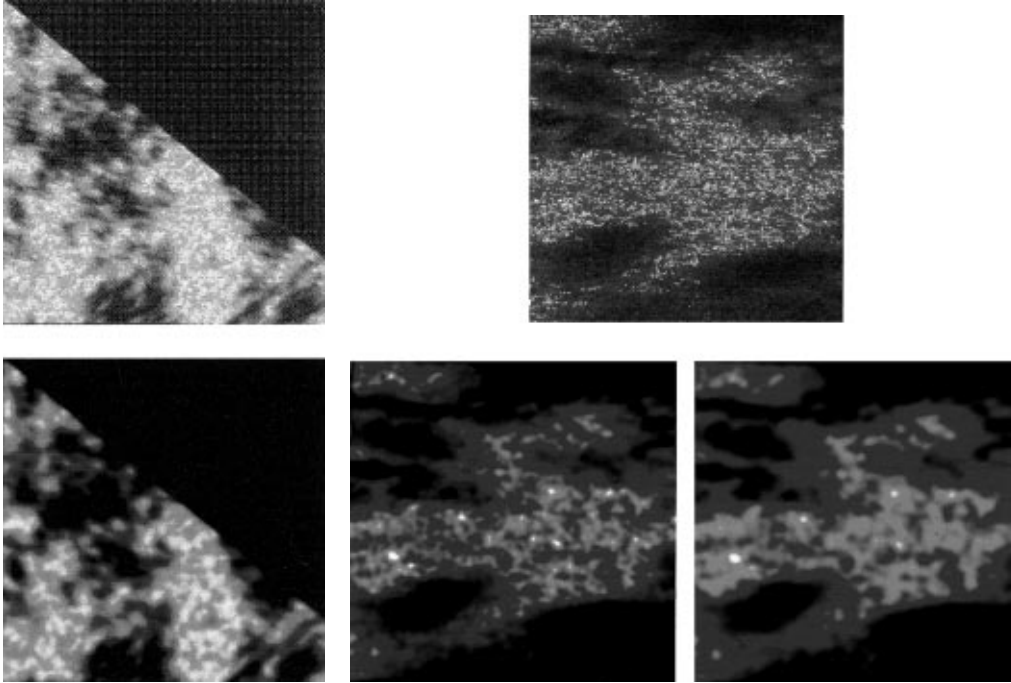


Fig. 3. Microscopic (upper frames) and macroscopic (lower frames) states of local galactic model at timesteps 200 **a)** and 500 **b)**; colour scheme: E : black; D : cyan; P : white; M : yellow; R : red; I : blue; L : green

$$a(Y; \tau; G) = a_o(Y; G) + (\tau - \tau_o) a'(Y; G), \quad (3.1)$$

where the subscript o refers to the onset of phase (ii), or more generally to any time sufficiently exceeding the lifetime of phase (i) of the galaxy. In our numerical experiments we have set $\tau_o = 100$; except for a few experiments involving small induced probabilities this value of τ_o corresponds to a reference time within the stationary phase.

The parameter dependence of the two expansion coefficients $a_o(Y; G)$ and $a'(Y; G)$ is determined from a series of test experiments. We represent this dependence by a linear ansatz written in the form

$$a_o(Y; G) = a_{or}(Y; G) + \sum_k (P_k - P_{kr}) \alpha_k(Y; G), \quad (3.2a)$$

$$a'(Y; G) = a'_r(Y; G) + \sum_k (P_k - P_{kr}) \alpha'_k(Y; G), \quad (3.2b)$$

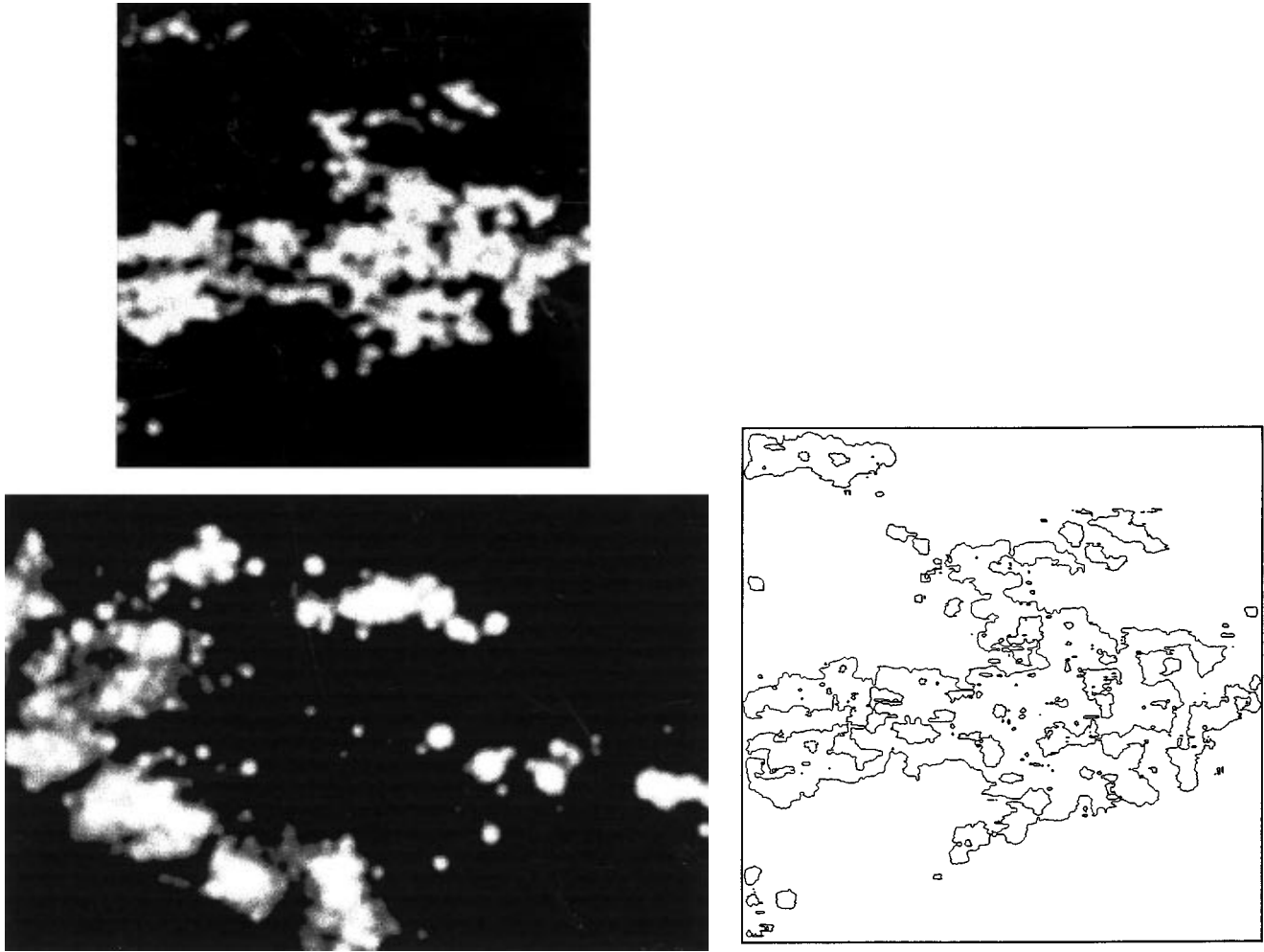


Fig. 4. **a)** Averaged state of local galactic model at timestep 500, for Gaussian smoothing; the grey level g is defined by $g = p\rho(P) + r\rho(R) + m\rho(M)$ (ρ , number densities < 1 estimated for the bright objects P , R and M ; $p : r : m = 10 : 2 : 1$); white: $g = 255$; black: $g = 0$; **b)** comparison with blow up of real HST photograph of M100; **c)** isophote at level $g=125$

where P_k is the transition probability of the k^{th} independent reaction step (notations of Table 1). A subscript r to a model quantity a_{or} , a'_r indicates the value taken by this quantity in the reference model defined by the transition probabilities ($P_k = P_{kr}$) given in Col. (b) of Table 1 (initial amount of dust 72%). The coefficients of the expansions (3.2), $a_{or}(Y; G)$, $a'_r(Y; G)$, and $\alpha_k(Y; G)$, $\alpha'_k(Y; G)$, listed in Table 2, are calibrated by a least squares fit to a grid of 24 experiments in which each parameter ranges from 1/3 to 3 times its reference value.

To test for the goodness of the fit we compared the actual values a_o and a' of the 24 calibration models with their linear estimates (Eqs. 3.2a,b). As a rule, provided that a_o is not too small ($\gtrsim 0.02$), the relative agreement is better than 20%. The linear ansatz (3.2a) is thus satisfactory. Inaccuracies occur in runs in which the quasi-stationary phase is not yet properly established at our reference timestep $\tau_o = 100$ (which occurs if P_1 or P_2 are too small). We observe also that for species L the pa-

rameter a_o is almost always well approximated (precision better than 10%). On the other hand, the rate parameters a' are accurately given by the linear estimate only for the inactive species I and L . For the remaining species the estimate may differ by as much as a factor of 2 or 3; within the accuracy of the linear ansatz (Eqs. 3.2a,b) it is therefore legitimate to disregard the P_k -dependence in the rates of the relative populations of the active species $A = P, M, R$: $a'(A; G) \approx a'_r(A; G)$.

The coefficient $\alpha_k(A; G)$ indicates how a variation around the reference model of the k^{th} reaction probability, ΔP_k , affects the quasi-stationary population of the active species A ($= P, M, R$); the induced variation of the relative population obeys $\Delta a(A; G) = \alpha_k(A; G)\Delta P_k$; hence, if $\alpha_k(A; G)$ is positive [negative], then species A is created [destroyed] — either directly or indirectly — in process k . We note that the magnitude of the sensitivity itself, $|\alpha_k(A; G)|$, is not only large in a direct creation or destruction process; it may remain so also in

indirect processes. As an example, the direct sensitivity of the protostar population to the probability of the direct star induced protostar formation process, $\alpha_3(P; G)$, is 0.27; the R population, although only indirectly affected by the same reaction, has a larger sensitivity, $\alpha_3(R; G) = 0.71$. Note that the sensitivities to spontaneous (gas and dust induced) star formation, $\alpha_1(P; G)$ and $\alpha_1(R; G)$, are much larger, 2.7 and 3.4 respectively; however, for all our runs the spontaneous transition probability P_1 itself is small (≤ 0.0015) in comparison with the star induced transition probability P_3 (≥ 0.033); accordingly the overall contribution of the spontaneous formation process ($P_1 - P_{1r}$) $\alpha_1(P; G)$ remains always negligible with respect to the star induced formation ($P_3 - P_{3r}$) $\alpha_3(P; G)$.

As already mentioned, an examination of the orders of magnitude of the fragments $(P_k - P_{kr}) \alpha_k(Y; G)$ entering the definition of the quasi-stationary relative population $a_o(Y; G)$ shows that some of them are negligible when the latter coefficient is recomputed for the calibration models. It is then reasonable to discard those fragments also in the general representation (3.2a). The P population, $a_o(P; G)$, is dominated by the contributions of star induced star formation, of direct and star induced decay processes of protostars into gas; star induced transformation of protostars into the M species also contribute; spontaneous P formation is negligible, and so are most of the indirect processes. For the M and R populations, $a_o(M; G)$ and $a_o(R; G)$, all steps yield essentially comparable orders of contribution. Negligible contributions $(P_k - P_{kr}) \alpha_k(Y; G)$ are listed in Table 2 in the form $\alpha_k(Y; G) = v \approx 0$, where v is the actual numerical value of the sensitivity as obtained in our calibration.

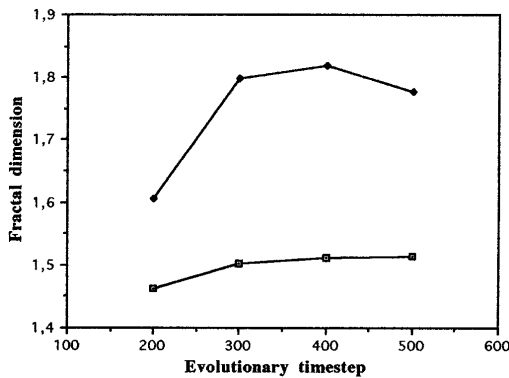


Fig. 5. Fractal (correlation) dimensions associated with the arm structure of synthetic photographs: dimension of the arm area (upper curve) and dimension of the arm border (lower curve)

At any timestep τ , the evolution of each one of the 6 formal species E, D, P, M, R, I, L is represented by a probabilistic transition (Table 1). For instance, for species R our model accounts for 3 transitions (regarded as mutually exclusive) translating the physical fact that a red giant ei-

ther remains a red giant, or it becomes an inert star, or it transforms into gas; 2 transition probabilities are independent. Since our model involves 21 transitions, or reactions (cf. Table 1) among 6 species, 15 transition probabilities are independent (P_1, P_2, \dots, P_{15} in Table 1).

Observationally we can determine 5 relative populations of species, $a(Y; \tau_{\text{gal}}; G)^{\text{obs}}$, $Y = P, M, R, I, L$. Substitution of Eqs. (3.2a,b) into Eq. (3.1) then yields the following linear system in the model parameters P_k

$$\sum_k [\alpha_k(Y; G) + \tau_{\text{gal}} \alpha'_k(Y; G)] P_k = a(Y; \tau_{\text{gal}}; G)^{\text{obs}} - [a_{\text{or}}(Y; G) + \tau_{\text{gal}} a'_{\text{or}}(Y; G)] + \sum_k [\alpha_k(Y; G) + \tau_{\text{gal}} \alpha'_k(Y; G)] P_{kr} \quad (3.3)$$

(5 equations in 15 unknowns). Further observational information is available from the spatial distribution of the different species. Our purpose is to show that in principle the latter can be quantified in a way as to supply additional constraining equations in the unknowns P_k .

4. The space structure

The simulation of a mere global evolution of the galactic species, summarised in a small number of *time series*, would not require a detailed CA model: The global evolution is satisfactorily reproduced by models of class (1), namely by the low order ODEs generated from a mean field approximation; the only extra information supplied by the CA model is a superposition of *statistical fluctuations* which mimic to some extent the genuine observable fluctuations.

The real interest of a CA approach is that it produces the detailed time behaviour of a complex *space dependence* of the physics of the galaxy (encoded in CA field variable $F(\tau; i, j)$). Due to the intrinsically highly involved spatial patterns, there seems to be no fully satisfactory way of exhibiting the information carried by this field variable in any data-compressed form. A proper appreciation of the full model results requires an analysis of the sequence of frames defined by the field matrices $F(0; i, j)$, $F(1; i, j)$, $F(2; i, j)$, ... by an animation technique; only this form of visualisation can properly reveal the local details of the dynamics.

In Fig. 3 we supply a first frame (a) showing the microscopic CA state $F(\tau; i, j)$ of the galactic region at timestep $\tau = 200$ in the auxiliary lattice L together with a space-averaged macroscopically meaningful picture of the same zone (Gaussian averaging over 2 pixels), and a second frame (b), at step $\tau = 500$ in the physical lattice L' together with a space-averaged picture (radius 2 and 4 pixels) (model parameters: column a of Table 1; initial conditions shown in Fig. 1). The intricacy of the averaged computed structure at any timestep τ leaves little hope

Table 2. Expansion coefficients $a_{or}(Y; G)$, $a'_r(Y; G)$, $\alpha_k(Y; G)$ and $\alpha'_k(Y; G)$

Reference	state	$\tau_o = 100$;	G :	whole	lattice
$a_{or}(P; G)$	0.127	$a'_r(P; G)$	-1.3×10^{-5}		
$a_{or}(M; G)$	0.113	$a'_r(M; G)$	-2.0×10^{-5}		
$a_{or}(R; G)$	0.0529	$a'_r(R; G)$	-2.4×10^{-5}		
$a_{or}(I; G)$	0.0019	$a'_r(I; G)$	2.6×10^{-5}		
$a_{or}(L; G)$	0.010	$a'_r(L; G)$	7.0×10^{-5}		
reaction 1: $D + dD \rightarrow P + dD$					
$\alpha_1(P; G)$	$2.75 \approx 0$	$\alpha'_1(P; G)$	-0.100		
$\alpha_1(M; G)$	48.5	$\alpha'_1(M; G)$	-0.140		
$\alpha_1(R; G)$	3.41	$\alpha'_1(R; G)$	-0.011		
$\alpha_1(I; G)$	0.043	$\alpha'_1(I; G)$	0.002		
$\alpha_1(L; G)$	-2.71	$\alpha'_1(L; G)$	-0.017		
reaction 2: $D + dD \rightarrow L + dD$					
$\alpha_2(P; G)$	$32.2 \approx 0$	$\alpha'_2(P; G)$	-0.32		
$\alpha_2(M; G)$	7.95	$\alpha'_2(M; G)$	-0.19		
$\alpha_2(R; G)$	-40.4	$\alpha'_2(R; G)$	-0.07		
$\alpha_2(I; G)$	-1.12	$\alpha'_2(I; G)$	-0.018		
$\alpha_2(L; G)$	59.4	$\alpha'_2(L; G)$	0.42		
reaction 3: $D + pP + mM + rR \rightarrow P + pP + mM + rR$					
$\alpha_3(P; G)$	0.268	$\alpha'_3(P; G)$	-3.8×10^{-4}		
$\alpha_3(M; G)$	0.174	$\alpha'_3(M; G)$	-4.0×10^{-4}		
$\alpha_3(R; G)$	0.714	$\alpha'_3(R; G)$	-1.0×10^{-4}		
$\alpha_3(I; G)$	0.0272	$\alpha'_3(I; G)$	3.5×10^{-4}		
$\alpha_3(L; G)$	-0.021	$\alpha'_3(L; G)$	-1.8×10^{-4}		
reaction 4: $P \rightarrow M$: not parametrised					
reaction 5: $P + mM + rR \rightarrow M + mM + rR$					
$\alpha_5(P; G)$	-1.42	$\alpha'_5(P; G)$	1.22×10^{-3}		
$\alpha_5(M; G)$	-0.130	$\alpha'_5(M; G)$	-3.2×10^{-4}		
$\alpha_5(R; G)$	4.10	$\alpha'_5(R; G)$	-1.3×10^{-3}		
$\alpha_5(I; G)$	0.130	$\alpha'_5(I; G)$	2.0×10^{-3}		
$\alpha_5(L; G)$	-0.027	$\alpha'_5(L; G)$	-3.8×10^{-4}		
reaction 6: $P + eE \rightarrow D + eE$					
$\alpha_6(M; G)$	-0.180	$\alpha'_6(M; G)$	1.5×10^{-4}		
$\alpha_6(R; G)$	0.036	$\alpha'_6(R; G)$	1.3×10^{-4}		
$\alpha_6(I; G)$	-6.1×10^{-5}	$\alpha'_6(I; G)$	2.0×10^{-5}		
$\alpha_6(L; G)$	9.0×10^{-3}	$\alpha'_6(L; G)$	6.4×10^{-5}		

Table 2. continued

reaction 7: $P + mM + rR \rightarrow D + mM + rR$			
$\alpha_7(P; G)$	-0.070	$\alpha'_7(P; G)$	5.9×10^{-4}
$\alpha_7(M; G)$	-0.487	$\alpha'_7(M; G)$	9.6×10^{-4}
$\alpha_7(R; G)$	-0.112	$\alpha'_7(R; G)$	-4.5×10^{-7}
$\alpha_7(I; G)$	-1.5×10^{-3}	$\alpha'_7(I; G)$	-5.5×10^{-5}
$\alpha_7(L; G)$	2.2×10^{-2}	$\alpha'_7(L; G)$	2.2×10^{-4}
reaction 8: $M \rightarrow R$: not parametrised			
reaction 9: $M + rR \rightarrow R + rR$			
$\alpha_9(P; G)$	0.251	$\alpha'_9(P; G)$	4.4×10^{-4}
$\alpha_9(M; G)$	-0.428	$\alpha'_9(M; G)$	6.8×10^{-4}
$\alpha_9(R; G)$	-0.272	$\alpha'_9(R; G)$	3.3×10^{-5}
$\alpha_9(I; G)$	-5.8×10^{-3}	$\alpha'_9(I; G)$	-1.3×10^{-4}
$\alpha_9(L; G)$	0.010	$\alpha'_9(L; G)$	1.1×10^{-4}
reaction 10: $M \rightarrow D$			
$\alpha_{10}(P; G)$	0.363	$\alpha'_{10}(P; G)$	1.4×10^{-4}
$\alpha_{10}(M; G)$	-0.593	$\alpha'_{10}(M; G)$	5.5×10^{-5}
$\alpha_{10}(R; G)$	-0.594	$\alpha'_{10}(R; G)$	4.3×10^{-4}
$\alpha_{10}(I; G)$	-0.020	$\alpha'_{10}(I; G)$	-2.8×10^{-4}
$\alpha_{10}(L; G)$	0.014	$\alpha'_{10}(L; G)$	1.6×10^{-4}
reaction 11: $M + mM + rR \rightarrow D + mM + rR$			
$\alpha_{11}(P; G)$	1.04	$\alpha'_{11}(P; G)$	2.4×10^{-3}
$\alpha_{11}(M; G)$	0.626	$\alpha'_{11}(M; G)$	2.5×10^{-3}
$\alpha_{11}(R; G)$	-1.96	$\alpha'_{11}(R; G)$	1.9×10^{-3}
$\alpha_{11}(I; G)$	-0.065	$\alpha'_{11}(I; G)$	-9.2×10^{-4}
$\alpha_{11}(L; G)$	0.015	$\alpha'_{11}(L; G)$	6.3×10^{-5}
reaction 12: $R \rightarrow D$			
$\alpha_{12}(P; G)$	$0.023 \approx 0$	$\alpha'_{12}(P; G)$	2.1×10^{-4}
$\alpha_{12}(M; G)$	0.104	$\alpha'_{12}(M; G)$	1.1×10^{-4}
$\alpha_{12}(R; G)$	-0.125	$\alpha'_{12}(R; G)$	1.1×10^{-4}
$\alpha_{12}(I; G)$	-4.9×10^{-3}	$\alpha'_{12}(I; G)$	-6.2×10^{-5}
$\alpha_{12}(L; G)$	4.5×10^{-3}	$\alpha'_{12}(L; G)$	9.1×10^{-6}
reaction 13: $R \rightarrow I$: not parametrised			
reaction 14: $L \rightarrow D$: not parametrised			
reaction 15: $L \rightarrow I$: not parametrised			

for a duplication of these results by a low order differential model, or even by a tractable PDE model.

Figure 4a is an attempt at generating a synthetic black and white photograph from the computed CA state at timestep 500; the grey level at each CA cell is defined through a weighted average of the contribution of the luminous matter (cf. caption); the final picture is a spatial Gaussian average over the ‘microscopic’ grey levels (radius = 2 pixels). The pattern of white patches is seen to match

almost exactly the lightblue areas in the averaged picture of Fig. 3b.

Figure 4b is a real HST photograph of a part of M100 of roughly same size as the computed galactic zone of Fig. 3b. Although both pictures are not comparable in detail — we should keep in mind that the synthetic figure represents a single realisation of a stochastic model — they do show one small-scale characteristic structural similarity: individual light patches in both pictures have statistically equivalent shapes.

In our model these patches correspond to regions of high concentrations of protostars; the existence of connected patches is related to the SPSF mechanism (and the Goldreich & Lynden–Bell (1965) chaotic mechanism).

Figure 4c gives the structure of the levels of constant brightness of the synthetic photograph.

From Figs. 3 and 4 we can infer several general conclusions on the space structure as generated in our models. If we accept the view that the most luminous objects (the population of protostars) are the tracers of the *galactic arms* (collection of bright patches in the synthetic photograph Fig. 4a), then our model generates arms exhibiting an irregular fragmented *local geometry* (on scales of the order of less than 200 pc); the *large scale geometry* (> 400 pc), on the other hand, appears to be channelled by the smooth dynamics of the galaxy (gravitation induced shearing effect of the stationary velocity field). The stabilised arm pattern tends to establish itself in the quasi-stationary regime (ii) of the global evolution of the species.

4.1. Small scale geometry

As a measure of the *local fragmentation* we have determined *fractal dimensions* associated with the arm structure. This can be done in several ways: The fractal dimension F of the boundary of the area occupied by the luminous objects (Fig. 3) in (a) the physical lattice L' ; and in (a') the auxiliary lattice L ; one could likewise directly measure the fractal dimension of synthetic isophotes (Fig. 4c). The natural method for estimating the fractal dimension F of a topologically linear set (border of the area occupied by a population A, or fixed isophote respectively) embedded in a plane, consists in measuring the length $l(\Delta r)$ of this set at different resolutions Δr ; the dimension $F \in [1, 2]$ is then related to the slope of the $\ln l(\Delta r) - \ln \Delta r$ relation, which is equal to $1 - F$ at a fine enough resolution (provided that this relation is linear for $\Delta r \rightarrow 0$). It is practically more convenient to estimate F via the *correlation dimension* (which is equal to the fractal dimension if the latter exists; cf. for instance Perdang 1990, 1991); this latter method has been adopted in our numerical work. Theoretically, since L' is a smooth deformation of L , the estimate of the fractal dimension is independent of the grid L or L' .

Table 3. Evolution of bulk dimension of arm structure

τ	F (in L')
200	1.61
300	1.80
400	1.82
500	1.78

This conclusion cannot be extended to arbitrary galactic dynamics. In the presence of a *chaotic flow field*, we should expect the latter to affect, and increase the fractal dimension of the arm structure. On the other hand, even in the case of a smooth velocity field, and hence a smooth transformation between the physical space and the auxiliary space, there is no guarantee that the actual technique of estimating the dimension does yield the same value in both cases. In fact, the $\ln l$ against $\ln \Delta r$ curve shows in practice a linear part over some Δr range, and it is the slope of the latter which estimates F ; at small scales, $\Delta r < \Delta r_o$ (= actual resolution of the figure: 5 to 10 cells), the $\ln l - \ln \Delta r$ curve flattens out; at large scales, $\Delta r > \Delta r_L$ (order of macroscale of structure in the figure < size of figure), the local slope of $\ln l - \ln \Delta r$ can take on arbitrary values. Under a nonlinear but smooth transformation of the figure, if the transformation itself exhibits structure over the range $(\Delta r_o, \Delta r_L)$, then the slope of the curve $\ln l' - \ln \Delta r'$ of the transformed figure will be affected over the transformed range of $(\Delta r_o, \Delta r_L)$. Although theoretically the fractal dimension as defined for $\Delta r \rightarrow 0$, remains the same in the original and transformed variables, practical estimates are bound to operate at finite resolutions $> \Delta r_o$. For instance, if we have a set of hierarchically distributed points on a straight line (so that $0 < F < 1$), experimentally approximated by a finite number of dots distributed according to a finite number of hierarchical levels, then a numerical estimate of the fractal dimension F on the experimental realisation in $(\Delta r_o, \Delta r_L)$ yields an acceptable theoretical estimate of F . However, suppose we perform a stretching of the experimental points, $x' = Sx$ (x , initial coordinate of a point on the line; x' new coordinate; S , stretching factor); if S is chosen such that the intrinsic resolution in the new coordinates, $\Delta r'_o = S\Delta r_o \geq \Delta r_L$, and if we estimate again the dimension F' from the slope of the $\ln l' - \ln \Delta r'$ curve, at small $\Delta r' (< S\Delta r_o)$, then we manifestly find $F' < F$; note that $F' \rightarrow 0$ for S large enough. This example should make it clear that an a priori knowledge of the actual intrinsic resolution of our experimental data is required to make a reliable numerical estimate of a fractal dimension.

The discrepancies in fractal dimension estimates of attractors in phase spaces referred to different variables (cf. Cannizzo et al. 1990 for stellar pulsation attractors) are related to this effect.

The fractal dimension F shown in Table 3 is a dimension of the *area* occupied by the arms rather than of the border of the arm region (or length of an isophote). The fact that this dimension turns out to be non-integer reflects here the fragmented and hierarchical topology of the arms; the number of arm fragments increases as we increase the resolution; this behaviour is in agreement with the observational situation (cf. the role of resolution in Fig. 1 of Paper I). The evolution of the dimension F exhibited corresponds to the run chosen for constructing the

synthetic photographs (parameter values of Col. (a) in Table 1). The effect of the comparatively low spontaneous star formation probability P_1 is to delay the onset of the catalytic star formation process. As a consequence, the establishment of the quasi-stationary state is delayed as well ($\tau_o \approx 300$ instead of 100 for the larger P_1 values). It transpires from Table 3 that the bulk fractal dimension is reasonably stationary ($F \approx 1.8$) beyond timestep 300.

The dimension given in Table 3 is the *correlation dimension* of the area occupied by the arm (cf. Perchang 1991); Fig. 5 also illustrates the behaviour of the fractal dimension of the border (estimated again through a correlation dimension) which, as expected, is lower than the previous dimension. Other fractal dimensions attached with the arms (mass dimension of arm area, mass dimension of border) have also been estimated; the latter may differ by 10% from the corresponding correlation dimensions; beyond step 300 all dimensions are essentially stationary (cf. Fig. 5).

It seems natural to expect that the *fine structure* of an arm (understood as the locus of the luminous objects) is directly related to the kinetics of stellar evolution, and more specifically to the star-induced star formation (transition probability P_3). Accordingly the fractal dimension of the arm structure should help constrain the range of the model parameters. If we summarise again the results of a collection of numerical experiments in an interpolation formula of type (3.2a) (disregarding here the time dependence), we obtain a constraining relation in the form (cf. Eq. (3.3) with the dashed parameters left out)

$$\sum_k \Phi_k P_k = F^{\text{obs}} - F_r + \sum_k \Phi_k P_{kr} \quad (4.1)$$

(F^{obs} , observational determination of the arm dimension for a real galaxy). However, a few test experiments have suggested that the dimensions of the arms are only marginally sensitive to the individual stellar processes. It would seem that once the stationary arm pattern is established, the arm structure acquires fairly universal fractal dimensions which are independent of the precise physics prevailing in the formation process of the arm. Such a picture is not inconsistent with the percolation phase transition describing the arm formation as proposed in GSS (cf. further comments in the next subsection).

In any event, our experiments are indicative that the knowledge of these dimensions does not provide any significant constraints on the transition probabilities parametrising stellar evolution.

4.2. Large scale structure

We can further infer from our simulations that the large scale pattern traced out by the arms has a twofold origin:

(i) It is due to the action of the *galactic dynamics* (the shear of the velocity field) on an initial inhomogeneous

gas distribution (empty bubbles in our simulation); the resulting smooth geometry is then irregularly modulated by the randomly acting physics of the star formation and evolution processes.

In our experiments we start with large size empty fragmented bubbles floating in an originally uniform gas configuration. Since, as indicated, the additional dynamic mechanism included in our treatment, namely diffusion, is inefficient over distances of the order of a fraction of the size of our lattice, any large scale deformation of a bubble is a consequence of a stretching by the inhomogeneous velocity field only. Through the stretching the bubble transforms into a single empty lane tending to become parallel to the shear direction; it transforms into a double lane once the stretched bubble has acquired a length exceeding the length of the ring it belongs to, etc. The action of the shear on several bubbles leads to a system of parallel empty lanes. Since no activity can occur in the empty regions, the bubbles define the interarm zone. Support of the observable arm, the zone filled with gas likewise acquires a shape of parallel arcs covering our lattice area.

This large scale scenario, in substance already described by Weizsäcker (1951) as a mechanism responsible for the formation of spiral structure in galaxies, is independent of any reaction kinetics.⁶

We convinced ourselves of the efficiency of this mechanism in the CA framework by running our simulation program with the evolutionary kinetics and diffusion turned off: Voids and matter are then observed to arrange in arms. Test runs further make it clear that the global shape of the arms is determined by the analytic form of the stationary velocity field. We mention in passing that theoretically the fractal dimension of the matter-void interface is here time independent (≈ 1.30 in our experiments); it is just fixed by the construction algorithm of the bubble; physically this dimension should then reflect the formation processes of the molecular clouds. In the actual simulation, however, the stretching transforms the initially irregular lines of constant density into almost straight lines along the shear direction. This is a consequence of a loss of spatial resolution accompanying the stretching transformation which, in principle, should reveal finer and finer details (cf. our previous remark). Hence, since the CA model is working with a finite resolution, a numerical estimate yields an apparent fractal dimension decreasing with time towards 1.

(ii) Carriers of the collection of luminous objects, the lanes of matter then naturally trace out an underlying large scale structure of progressively smoother geometry on which the observable brightness patterns of the galaxy

⁶In a paper with Heisenberg, the validity of this idea was substantiated by a simulation in which an elongated irregular 2D cloud of dots is rotated about an inner point of the cloud, according to Kepler's third law. The cloud then develops into a regular two-armed spiral (Heisenberg & von Weizsäcker 1948).

are superimposed (Fig. 4a). As already recalled, GSS have interpreted the onset of the formation of a bright arm as a *percolation phase transition* leading to the occurrence of a ‘connected infinite cluster’ of active stars. Their model makes use of a single control parameter, p (probability of induced star formation, i.e. counterpart of our parameter P_3); the phase transition occurs for $p > p_c$, c a critical value.

The analogue of the GSS percolation transition is observed in our more elaborate model, the cluster being identified by the protostar population. We mention that at fixed reaction probabilities the initial fraction of gas, $f(D)$, can likewise be chosen as a relevant control parameter for the phase transition: An ‘infinite’ cluster develops as $f(D)$ exceeds a critical value $f_{\text{crit}}(D)$ (≈ 0.66 for the choice of reaction parameters in Lejeune 1993).

The value of the critical control parameter (p , P_3 or $f(D)$) eventually depends on an arbitrary convention of what we understand by ‘connection’ of 2 neighbouring cells. To illustrate this point, define two cells as being c -connected if they are less than c cells apart; a ‘cluster’ is then a collection of c -connected cells. It is manifest that the onset of the transition and the critical value of the control parameter depend on the specific arbitrary choice of c .

This remark is indicative that a practically relevant concept of ‘percolation’ for the galactic context must be predicated on the observational *resolution* (of which the parameter c is a caricature). The formal percolation concept as introduced in GSS has no directly accessible quantitative observational counterpart. The resolution dependence of the ‘connected infinite cluster’ can be demonstrated by image analysis of synthetic photographs (Figs. 4a,b) and real photographs (cf. Fig.1 in Paper I): As we increase the smoothing effect and generate lower resolution images, we observe more extended connected bright areas.

The GSS interpretation has the virtue, in our opinion, of supplying a *qualitative explanation* of the formation process of the bright arm structure in the galaxy by relating it to the statistical mechanics of percolation. The luminous arm structure (i.e. the extended connected patches covered by protostars and luminous objects in general) appear or disappear, as some fixed combination of the parameters regulating the evolution of galactic components goes through a critical value. On the account of the arbitrariness involved in the definition of the ‘percolation cluster’, it is hard to see, however, how the GSS percolation concept could help extract *quantitative information* on the stellar processes from galactic observations. In fact, if the transition is a genuine percolation phase transition, then the relevant information it does supply is that it carries *no* quantitative information on the specific physical mechanisms of the underlying model: The numerical coefficients characterising a real percolation phase transition

(critical exponents ν and γ ; cf. Eqs. (1.3) of Paper I), are *universal*, i.e. determined by global topological and geometrical factors (dimensionality and lattice symmetry); they are independent of the precise physics responsible for the formation of the cluster (exact evolutionary steps and corresponding transition probabilities). In view of this remark global parameters quantifying the arm structure are not used as constraints for the physics of our model. The fractal dimensions F already mentioned seemingly belong into this category as well.

Since our model involves several species of luminous objects (P , M and R), a phase transition is possible in principle for each of these species. We have traced such a situation under the conditions of an oscillatory regime. Extended areas of the galaxy then undergo cyclical changes: $P \rightarrow M \rightarrow R \rightarrow P \rightarrow \dots$. If realisable in genuine galaxies — the regime requires ranges of the transition probabilities probably not consistent with realistic galactic conditions — the physical nature of the luminous arm would cyclically change, from a predominantly protostar composition, to a main sequence and red giant composition.

Whether the transition isolated by GSS is to be viewed as a genuine percolation phase transition remains to be substantiated, even though the power-law behaviour of the cluster size characteristic for percolation has been verified under various conditions (cf. Lejeune 1993). In fact, a percolation phase transition, in its standard acceptance, describes a transition between *static states* under a quasi-static change of a control parameter (transition from absence of a percolation cluster to presence of a cluster); the notion of percolation involves no dynamics (cf. Stauffer 1985). In the present physical problem, we rather observe a propagation, i.e. a *dynamic phenomenon*, with the infinite cluster developing in time. Accordingly, the transition appears to be more closely related to what has been referred to as *self-organised criticality* (Bak et al. 1987-1989), a transition towards a dynamical state in which very large numbers of degrees of freedom are excited. Near the onset of self-organised criticality power-law dependences hold for various magnitudes attached with the clusters of excited degrees of freedom (distribution of cluster sizes, distribution of lifetimes of clusters, etc). To the best of our knowledge, and in contrast with the power-laws related with percolation, there has been no proof so far that the exponents of these laws are universal. Accordingly, if the identification of the infinite cluster formation with a transition to self-organised criticality applies in our case, then the exponents could carry additional information on the physics.

4.3. Space distribution of the luminous objects

An inspection of the picture of the cellstates (Fig. 3) indicates that the overall space distribution of the luminous objects, P , M and R is not homogeneous over the area investigated. The luminous objects appear to be

concentrated over lower-dimensional subsets, and this type of inhomogeneity is inherited by the inert objects I . As a consequence of their formation mechanism (cf. Table 1), the low mass stars L , on the other hand, are regularly scattered over the area originally covered by gas; but since the latter itself is not uniform, the L distribution inherits the lack of uniformity of the gas.

Physically the spatial distribution of a given species is determined by a combination of three effects: (a) the initial configuration; (b) the mechanisms of formation and destruction of this species; (c) the galactic kinematics (overall velocity field, and diffusion). On the assumption that the initial conditions are essentially the same for the class of galaxies under consideration, and under the proviso that we concentrate on small enough zones of these galaxies (over which the kinematic stretching effects are inefficient), we are entitled to expect that information on the transition probabilities P_k can be extracted from conveniently chosen parameters describing the spatial distribution of the species.

We have attempted to quantify the following single aspect of the space pattern traced out by the species P , M , R and I . It is a well known fact that in CA models individual states are often uniformly distributed over self-similar, or statistically self-similar sets (cf. Perdang 1993 Sect. 4 for an analytic discussion of several examples). Therefore, we have addressed the somewhat broader question of whether a mass dimension of the set covered by species Z ($= P, M, R, I$) does exist; if so, this fractal dimension can serve the purpose of a constraint for the transition probabilities P_k . To this end we test whether a scaling relation of the form

$$N(Z; i, j; G(r)) = C r^{f(Z)}, \quad \text{for } r \text{ small,} \quad (4.2)$$

is applicable to our experiments; here $N(Z; i, j; G(r))$ is the number of cells in state Z in a disc $G(r)$ centred at an arbitrary cell (i, j) of the auxiliary lattice L , or of the physical lattice L' ; the mass dimension $f(Z)$ ($\in [0, 2]$) exists provided that the interpolation coefficients C and $f(Z)$ of the experimental data are independent of the reference cell (i, j) . In the standard numerical method of estimating $f(Z)$ in our CA experiments differences in lattice L and L' may arise as a consequence of the stretching and accompanying loss of space resolution in L' (cf. our previous remarks). As already argued, under the loss of accuracy due to a large enough stretching in one direction a numerical estimate of $f(Z)$ in L' will be artificially reduced as compared to the estimate in L .⁷

⁷Test experiments have confirmed this point. For the model corresponding to our synthetic photographs we have in L' : $f(P) = 1.60$; $f(M) = 0.87$; $f(R) = 0.36$ and $f(I) = 0.10$ at step 200 (compare with Table 4); the large differences in the case of the M and R species are due to an additional inaccuracy related to the small population of these objects. We have computed

Table 4. Fractal dimensions of space distributions for species P , M , R and I

τ	$F(P)$	$F(M)$	$F(R)$	$F(I)$
200	1.72	1.50	1.03	0.14
500	1.85	1.63	1.34	0.76

Table 4 exhibits the conclusion of our test. It shows that numerical values of f do indeed exist (plots of $\ln N$ against $\ln r$ indicate a broad linear interval, and the slope is independent of the central cell). The f values supplied in the Table are all computed in the auxiliary lattice L in order to avoid the loss of local accuracy accompanying the stretching in L' . We believe that this procedure provides the closest theoretical approximation to an observational mass dimension as given in the frame of the observer, provided only that the observational estimate is made over a small part of a high resolution photograph (with $G(r)$ larger than the actual resolution).

The mass dimension for the different species does show a significant dependence on the model parameters. In the quasi-stationary phase (ii) this dimension is practically time independent. Again, the apparently exceptional behaviour of the model on which our synthetic photographs are based, which exhibits a noticeable increase in f between timesteps 200 and 500, is due to the fact that the onset of quasi-stationarity is delayed. We approximate the mass dimensions over phase (ii) by the linear ansatz

$$f(Z; \tau) \simeq f_o(Z) = f_{\text{or}}(Z) + \sum_k (P_k - P_{k\tau}) \phi_k(Z), \quad (4.3)$$

($Z = P, M, R, I$). The reference values $f_{\text{or}}(Z)$ correspond to the model whose parameters are listed in Col. b of Table 1; the collection of expansion coefficients $\phi_k(Z)$ supplied in Table 5 have been obtained from 15 calibration models whose parameters P_k scatter around the reference model.

The counterpart of Eq. (3.3) becomes here

$$\sum_k \phi_k(Z) P_k = f(Z)^{\text{obs}} - f_{\text{or}}(Z) + \sum_k \phi_k(Z) P_{k\tau}, \quad (4.4)$$

also the *correlation dimension* (cf. Perdang 1991) of the distribution of the different species; we find that as a rule, the latter is smaller than the mass dimension, obeying approximately the relation $f(Z) - 0.1$. Since in the correlation dimension we sum over all pairs of identical states, this measure includes here the effect of the input inhomogeneity in the matter distribution (presence of empty bubbles); the mass dimension is estimated at positions where matter is actually present. In our context both measures refer to different aspects of the distributions.

($Z = P, M, R, I$). Hence, given the observational estimates of the current fractal dimensions of the distribution of the different species P, M, R, I in a given galaxy (assumed to be in the stable phase ii), $f(Z)^{\text{obs}}$, relations (4.4) provide 4 additional linear constraining equations for the model parameters P_k .⁸

5. Estimate of the free parameters

Our analysis has isolated 9 observational constraints in the form of algebraic equations (Eqs. 3.3 and 4.4) to be satisfied by our 15 a priori free model parameters P_k . If 6 additional constraints were available, the proposed CA formulation would have the status of a strictly phenomenological or empirical model, analogous to a Fourier representation for the simulation, the interpolation and the extrapolation of a time series. On the theoretical side, since a subset of the model parameters are recoverable from stellar evolution theory, our CA model could serve the purpose of testing current stellar evolution theory.

With 6 constraints being missing, we regard the latter subset, namely the transition probabilities of isolated objects, ($P[P; M] = P_4$; $P[M; R] = P_8$; $P[R; I] = P_{13}$; $P[L; I] = P_{15}$), as being given. The timescales of these processes flow from evolution theory and are converted into transition probabilities provided only that the stellar mass function be known.

If we consider timescales less than a few Gy, then the decay probabilities of the low mass stars become negligible, and we may set further $P[L; D] = P_{14} \approx 0$ (together with $P[L; I] = P_{15} \approx 0$). Moreover, as already pointed out, the spontaneous star formation rate, $P[D; P] = P_1$, has only a minor influence on the abundance of the protostar species (except for the delay effect mentioned). In all cases the star-induced star formation rate is the dominant mechanism. We believe therefore that we can reasonably fix the specific parameter P_1 . The numerical value

⁸We have pointed out above that the critical exponents referring to the percolation phase transitions are universal and therefore they do not carry any information on the physics. Since critical exponents are fractal dimensions in disguise, the question arises whether conversely the fractal dimensions attached with the geometric sets of the different species are not intrinsically universal themselves. In fact, as observed elsewhere (Perdang 1993), in analytically solvable CA models over square lattices only specific dimensionalities turn up for the carriers of individual states. It is not impossible then, that the parameter and time dependences we observe in the numerically determined fractal dimensions of the galactic simulation merely reflect the fact that a true fractal structure is not yet achieved. However, even if it were not a genuine fractal dimension, $f(Z)$ then would remain a quantitative index characterising the space distribution of species Z . A valid model for a given galaxy must duplicate the observational value of this index. We believe, therefore, that even under those circumstances the observational estimates of the exponents $f(Z)$ continue to carry information about the free parameters of our model.

Table 5. Expansion coefficients f_{or} and $\phi_k(Z)$ (Eq. 4.4)

$f_{\text{or}}(P)$	1.89			$f_{\text{or}}(M)$	1.91				
$f_{\text{or}}(R)$	1.90			$f_{\text{or}}(I)$	1.88				
<hr/>									
D	+	dD	\rightarrow	P	+	dD	$D + dD$	\rightarrow	$L + dD$
$\phi_1(P)$		78.1				$\phi_2(P)$			137.6
$\phi_1(M)$		58.5				$\phi_2(M)$			191.3
$\phi_1(R)$		33.0				$\phi_2(R)$			271.4
$\phi_1(I)$		160.5				$\phi_2(I)$			502.5
<hr/>									
$D + pP + mM + rR \rightarrow P + pP + mM + rR$						P	\rightarrow	M	
$\phi_3(P)$		0.474				not parametrised			
$\phi_3(M)$		0.382				not parametrised			
$\phi_3(R)$		0.652				not parametrised			
$\phi_3(I)$		2.495				not parametrised			
<hr/>									
$P + mM + rR \rightarrow M + mM + rR$						$P + eE \rightarrow D + eE$			
$\phi_5(P)$		0.286				$\phi_6(P)$			-0.273
$\phi_5(M)$		-0.786				$\phi_6(M)$			-0.293
$\phi_5(R)$		-1.081				$\phi_6(R)$			-0.238
$\phi_5(I)$		2.994				$\phi_6(I)$			0.645
<hr/>									
$P + mM + rR \rightarrow D + mM + rR$						M	\rightarrow	R	
$\phi_7(P)$		-1.080				not parametrised			
$\phi_7(M)$		-1.029				not parametrised			
$\phi_7(R)$		-1.403				not parametrised			
$\phi_7(I)$		-6.710				not parametrised			
<hr/>									
$M + rR \rightarrow R + rR$						$M + rR \rightarrow M + rR$			
$\phi_9(P)$		-0.633				$\phi_{10}(P)$			-1.576
$\phi_9(M)$		-0.526				$\phi_{10}(M)$			-2.150
$\phi_9(R)$		-0.909				$\phi_{10}(R)$			-3.451
$\phi_9(I)$		-3.926				$\phi_{10}(I)$			-13.73
<hr/>									
$M + mM + rR \rightarrow D + mM + rR$						R	\rightarrow	D	
$\phi_{11}(P)$		-3.631				$\phi_{12}(P)$			-0.016
$\phi_{11}(M)$		-4.912				$\phi_{12}(M)$			-0.075
$\phi_{11}(R)$		-8.285				$\phi_{12}(R)$			-0.263
$\phi_{11}(I)$		-32.83				$\phi_{12}(I)$			-1.140
<hr/>									
$R \rightarrow I$						$L \rightarrow D$			
		not				parametrised			not parametrised
<hr/>									
$L \rightarrow I$									
		not				parametrised			

we adopt is the value of the reference model (Col. (b) of Table 1). Within this framework of approximations we are then left with the following list of 9 parameters

$$(P_2, P_3, P_5, P_6, P_7, P_9, P_{10}, P_{11}, P_{12}). \quad (5.1)$$

The constraints we have discussed in the previous sections enable us then to derive these parameters directly from observation, namely (i) from relative mass fractions of the galactic components, and (ii) from fractal dimensions of the space distributions of the components.

6. Conclusion and outlook

We believe that our experiments provide arguments that the galactic arm structure results from a combination of two physical ingredients which have already been isolated separately in models of class (2) (cf. the Heisenberg–Weizsäcker simulation, 1948), and in the simplest models of class (3) (3–state CA experiments of MA and GSS). The two ingredients, rather than being mechanisms associated with what seemed to be regarded as rival theories, appear here not only as complementary, but as simultaneously necessary for the development of a realistic structure of a luminous arm pattern:

On the one hand, the overall large scale pattern of the *matter distribution* — the Grand Design — is determined by the gravitation induced general flow field (the differential rotation in a lowest order approximation). This structure is derivable from classical N –body experiments.

On the other hand, the *brightness distribution*, as directly accessible by photographs, reflecting the distribution of the bright components, is the immediate outcome of star formation and evolution processes. Since the latter processes occur in regions of high matter density, the high density regions are the carriers of the brightness distribution. The visible arm pattern, while then globally shaped by the matter distribution, possesses a structure of its own conditioned by the kinetics of star formation and evolution, which is superposed on the overall density distribution. The small scale structure of the brightness distribution is chiefly determined by this ‘chemical kinetics’.

We believe that this is the main conclusion of our analysis. It is borne out by a comparison of our synthetic photographs (Fig. 4a) with the pictures of real galaxies (HST photograph of NGC 4321, Fig. 4c, or enhanced AG photograph of NGC 5457, Fig. 1 of Paper I).

We are well aware that our treatment of the galactic dynamics in terms of a stationary velocity field in a rotating reference frame is not fully satisfying. It ignores not only a feedback of stellar evolution on the dynamics, but above all it discards the alternative of a chaotic flow in the region under investigation. It is indeed obvious that chaos in the dynamics must affect both qualitatively and quantitatively the large scale and the small scale pattern of the arms. Dynamical chaos is expected to increase the fragmented character of the visible arm structure, and presumably could become measurable via fractal dimensions of the arms. The ideal model of galactic structure should therefore not divorce the dynamics from star formation and evolution. In principle, to the extent that gravitation can be treated as an external force (as it is essentially done in standard self-consistent dynamic models; cf. for instance the model by Patsis et al. 1991), the gravitational effects could be incorporated in the CA model in a formally straightforward way. Unfortunately, such a procedure is highly time consuming.

The second quantitatively relevant aspect of our model is that it demonstrates that global observational galactic data contain easily accessible information on stellar evolution rates (including mass loss). We find that the 9 model parameters (5.1) are determined by a system of 9 equations which can be approximated by linear equations (Eqs. 3.3, 4.4) whose coefficients are observable. Four among the latter are *fractal dimensions* associated with the spatial distribution of the galactic species; while not yet available, there should be no major difficulty in deriving them from surveys of nearby galaxies. We hope to address this problem in the future. The remaining parameters are *mass fractions* of the different galactic components which can be found in the literature. Tables 2 and 3 provide a list of tentative input coefficients to carry out the inversion problem. It would be useful to recalibrate these coefficients, using a more extended array of test models covering also wider ranges of transition probabilities.

Finally, we should keep in mind that the artificial construction of the initial state as incorporated in our program should be replaced by a simulation of a physically more realistic process of molecular cloud formation (aggregation model, for instance). Detailed physics of star formation may be implemented as well, such as a simulation of a hierarchical fragmentation process of the cloud complex. Standard hydrodynamic simulations indicate in fact that the isothermal collapse of rotating dense clouds may lead to a succession of levels of condensations in condensations (Boss 1991). Such a mechanism could enhance local irregularities in the arm structure, thereby leading to a higher dimension F of the arm pattern. We plan to address these questions in a later work.

Acknowledgements. The authors are indebted to G. Barbaro for vital information on the parameters of stellar evolution, to H. Robe for his careful reading of a first version of this paper, and to J.P. Swings for providing them with an early HST photograph of M100. They wish to thank the referee Dr. Comins for his comments which helped improve the presentation of this paper. J.P. gratefully acknowledges a Royal Society – FNRS European Exchange Fellowship and financial support from the FNRS (Belgium).

References

- Bak P., Tang C., Wiesenfeld K., 1987, Phys. Rev. Lett. 59, 381
- Bak P., Tang C., Wiesenfeld K., 1988, Phys. Rev. A38, 364
- Bak P., Chen K., Creutz M., 1989, Nat 342, 780
- Boss A.P., 1991, Nat 351, 298
- Cannizzo J., Goodings D., Mattei J.A., 1990, ApJ 357, 235
- Feller W., 1971, An Introduction to Probability Theory and its Applications, Vol. II. Wiley, New York
- Gerola H., Seiden P.E., 1978, ApJ 223, 129 (quoted as GSS)
- Gerola H., Seiden P.E., Schulman L.S., 1980, ApJ 242, 517 (quoted as GSS)
- Glansdorff P., Prigogine I., 1971, Thermodynamic Theory of Structure, Stability and Fluctuations. Wiley, London, Chaps. XIV and XV

- Goldreich P., Lynden-Bell D., 1965, MNRAS 130, 125
- Heisenberg W., von Weizsäcker C.F., 1948, Z. Phys. 125, 290
- Herrmann H.J., 1983, J. Phys. A16, L611
- Lejeune A., 1993, in: Cellular Automata: Prospects in Astrophysical Applications. In: Perdang J.M., Lejeune A. (eds.), World Scientific, Singapore, p. 323
- Lejeune A., Perdang J., 1991, in: Computational Physics. In: Tenner A. (ed.), World Scientific, Singapore, p. 407
- Mueller M.W., Arnett W.D., 1976, ApJ 210, 670 (quoted as MA)
- Patsis P.A., Contopoulos G., Grosbol P., 1991, A&A 243, 373
- Perdang J., 1990, Vistas Astron. 33, 249
- Perdang J., 1991, in: Applying Fractals in Astrophysics, Lecture Notes in Physics m3. Springer, Berlin. p. 1
- Perdang J., 1993, in: Cellular Automata: Prospects in Astrophysical Applications. In: Perdang J.M., Lejeune A. (eds.), World Scientific, Singapore, p. 3
- Perdang J., 1996, A Family of Endogenous Growth Models (in preparation)
- Perdang J., Lejeune A., 1996, (Paper I)
- Sandage A., Tammann G.A., 1981, A Revised Shapley-Ames Catalog of Bright Galaxies, Carnegie Institute of Washington Publication 635, Washington D.C. (quoted as RSAC)
- Sandage A., Bedke J., 1988, Atlas of Galaxies, NASA SP-496, Washington D.C. (quoted as AG)
- Schulman L.S., Seiden P.E., 1983, Ann. Israel Phys. Soc. 5, 251 (quoted as GSS)
- Schulman L.S., Seiden P.E., 1986, Sci 233, 425 (quoted as GSS)
- Schulman L.S., 1993, in: Cellular Automata: Prospects in Astrophysical Applications. In: Perdang J.M., Lejeune A. (eds.), World Scientific, Singapore, p. 294 (quoted as GSS)
- Seiden P.E., 1985, in: The Milky Way Galaxy, IAU Symposium 106. In: van Woerden H., Allen R.J., Burton W.B. (eds.). Reidel, Dordrecht (quoted as GSS), p. 551
- Seiden P.E., Gerola H., 1979, ApJ 233, 56 (quoted as GSS)
- Seiden P.E., Gerola H., 1982, Fundam. Cosmic Phys. 7, 241 (quoted as GSS)
- Seiden P.E., Schulman L.S., 1990, Adv. Phys. 39, 1 (quoted as GSS)
- Seiden P.E., Schulman L.S., Gerola H., 1979, ApJ 232, 702
- Seiden P.E., Schulman L.S., Feitzinger J.V., 1982, ApJ 253, 91 (quoted as GSS)
- Stauffer D., 1985, Introduction to Percolation Theory, Taylor and Francis, London
- von Weizsäcker C.F., 1951 in: Festschrift zur Feier des zweihundertjährigen Bestehens der Akademie der Wissenschaften in Göttingen, Mathematisch-Physikalische Klasse. Springer, Berlin, p. 86